

## Article

# Cellulose Triacetate-Based Mixed-Matrix Membranes with MXene 2D Filler—CO<sub>2</sub>/CH<sub>4</sub> Separation Performance and Comparison with TiO<sub>2</sub>-Based 1D and 0D Fillers

Chhabilal Regmi<sup>1,2,\*</sup>, Jalal Azadmanjiri<sup>3</sup>, Vipin Mishra<sup>4</sup>, Zdeněk Sofer<sup>3</sup>, Saeed Ashtiani<sup>1</sup>  and Karel Friess<sup>1,\*</sup> 

<sup>1</sup> Department of Physical Chemistry, University of Chemistry and Technology, Technická 5, 16628 Prague 6, Czech Republic

<sup>2</sup> Department of Chemical Engineering, University of Arkansas, Fayetteville, AR 72701, USA

<sup>3</sup> Department of Inorganic Chemistry, University of Chemistry and Technology, Technická 5, 16628 Prague 6, Czech Republic

<sup>4</sup> Department of Glass and Ceramics, University of Chemistry and Technology, Technická 5, 16628 Prague 6, Czech Republic

\* Correspondence: regmic@vscht.cz (C.R.); friessk@vscht.cz (K.F.)

**Abstract:** Mixed-matrix membranes (MMMs) possess the unique properties and inherent characteristics of their component polymer and inorganic fillers, or other possible types of additives. However, the successful fabrication of compact and defect-free MMMs with a homogeneous filler distribution poses a major challenge, due to poor filler/polymer compatibility. In this study, we use two-dimensional multi-layered Ti<sub>3</sub>C<sub>2</sub>T<sub>x</sub> MXene nanofillers to improve the compatibility and CO<sub>2</sub>/CH<sub>4</sub> separation performance of cellulose triacetate (CTA)-based MMMs. CTA-based MMMs with TiO<sub>2</sub>-based 1D (nanotubes) and 0D (nanofillers) additives were also fabricated and tested for comparison. The high thermal stability, compact homogeneous structure, and stable long-term CO<sub>2</sub>/CH<sub>4</sub> separation performance of the CTA-2D samples suggest the potential application of the membrane in bio/natural gas separation. The best results were obtained for the CTA-2D sample with a loading of 3 wt.%, which exhibited a 5-fold increase in CO<sub>2</sub> permeability and 2-fold increase in CO<sub>2</sub>/CH<sub>4</sub> selectivity, compared with the pristine CTA membrane, approaching the state-of-the-art Robeson 2008 upper bound. The dimensional (shape) effect on separation performance was determined as 2D > 1D > 0D. The use of lamellar stacked MXene with abundant surface-terminating groups not only prevents the aggregation of particles but also enhances the CO<sub>2</sub> adsorption properties and provides additional transport channels, resulting in improved CO<sub>2</sub> permeability and CO<sub>2</sub>/CH<sub>4</sub> selectivity.

**Keywords:** cellulose triacetate; mixed-matrix membrane; MXene; TiO<sub>2</sub> nanoparticles; TiO<sub>2</sub> nanotube; gas separation



**Citation:** Regmi, C.; Azadmanjiri, J.; Mishra, V.; Sofer, Z.; Ashtiani, S.; Friess, K. Cellulose Triacetate-Based Mixed-Matrix Membranes with MXene 2D Filler—CO<sub>2</sub>/CH<sub>4</sub> Separation Performance and Comparison with TiO<sub>2</sub>-Based 1D and 0D Fillers. *Membranes* **2022**, *12*, 917. <https://doi.org/10.3390/membranes12100917>

Academic Editors: Liliana C. Tomé, Isabel Coelho and Luisa A. Neves

Received: 14 August 2022

Accepted: 16 September 2022

Published: 22 September 2022

**Publisher's Note:** MDPI stays neutral with regard to jurisdictional claims in published maps and institutional affiliations.



**Copyright:** © 2022 by the authors. Licensee MDPI, Basel, Switzerland. This article is an open access article distributed under the terms and conditions of the Creative Commons Attribution (CC BY) license (<https://creativecommons.org/licenses/by/4.0/>).

## 1. Introduction

Membrane-based gas separation has been recognized as a feasible and effective technology at the laboratory and industrial scales. Likewise, it has attracted eminent attention as the major paradigm for separation [1]. Application of this technology demonstrates it is competitive with and can complement traditional separation techniques due to its compounded properties, which include a rapid mass transfer rate, a specific gas-selective nature, lower power consumption rate, cheapness, and environmental benignity, among others [2]. However, in assessing the performance of polymers as membranes, a strong antithetical relationship between permeability and selectivity is persistently encountered [3]. The selectivity–permeability trade-off—a known bottleneck of polymeric membranes in the gas separation process—has been resolved through the development of MMMs [4]. An MMM utilizes the advantages of both polymeric and inorganic materials, thus potentially providing improved performance without significantly increasing the fabrication cost [5].

Active research into the design and synthesis of new materials via incorporation of inorganic nanoparticles has been extensively carried out in recent years. One of the latest approaches includes the inclusion of such particles into polymeric membranes to increase membrane performances such as permeability, selectivity, strength, and hydrophilicity [6–8]. Thus, the advancement in MMMs subsequently depends, in turn, on the development of suitable inorganic filler materials [9]. A vast number of nanomaterials, such as zeolites, metal–organic frameworks (MOF), carbon nanotubes, graphene sheets, activated carbon, carbon molecular sieves, and metal oxides [10,11] have been widely incorporated into a polymeric matrix to fabricate MMMs. These filler particles possess different sizes and shapes, most commonly 0D, 1D, and 2D. Such materials offer a promising strategy for the construction of membranes with a tailored pore structure and well-defined pore size distribution, substantially favoring elevated permeability and selectivity [1]. Although every preparation uses inorganic fillers, the resulting morphology and membrane separation performance can vary significantly, primarily due to the different capabilities of these molecular sieves—either based on shape or size—in discriminating various components available in the feed mixture [6]. A difference in the structure and characteristics of fillers may eventually give rise to a difference in the separation efficiency of the resulting MMMs. Similarly, the inclusion of filler particles can also result in alterations to the properties of the neighboring polymer phase. In contrast, polymers can increase the filler density, which ultimately affects the overall membrane separation performance [12].

Notwithstanding the benefits of the MMM-based separation process, many challenges still need to be confronted to enable the large-scale industrial implementation of such membranes [13]. A key challenge is characterizing the transport of species across the membrane and its dependence on inherent filler–matrix properties. Among others, 2D inorganic materials have evoked predominant attention in gas separation processes. These fillers possess sheet-like structures with atomic-level size and thickness, allowing them to be utilized in constructing transport channels of resultant gas separation membranes [14,15]. Similarly, the barrier created by such layered materials allows for discriminatory transfer of different gases through the membrane based on size sieving and/or electrostatic repulsion. Furthermore, their ultra-thin thickness can facilitate the transport of molecules or ions while perpetuating a preferable blocking effect. Thus, the design of nanochannels with 2D molecular sieve materials has aroused considerable interest and efforts [1]. The sheet-like fillers are either randomly distributed or align themselves (more or less) parallel to the membrane surface after their incorporation into the polymer matrix. This arrangement ultimately distorts the diffusion paths, thus increasing membrane selectivity by creating relatively higher resistance to larger molecules [4,16]. Similarly, these post-formed channels also lead to a gas barrier effect, counteracting the increase in gas permeability [17]. Instead, a pre-structured material such as MXene, which possesses intrinsically uniform effective channels, prevents uncontrollable packing during membrane preparation, thereby potentially and directly affecting the membrane separation performance [18]. The versatile chemistry of MXenes, a 2D layered material, has already been applied in different applications, including energy storage, biosensors, lubricating agents, and catalysis [1]. Therefore, the coupling of membrane separation technology with MXene is an emerging area of application. Although graphene oxide [19] and MoS<sub>2</sub> [20] have attracted plenty of interest in the membrane community, one of the essential advantages of MXenes, compared with these oxides, is their higher compatibility with the polymer matrix [21].

Similarly, layered atomic structures constructed on covalent bonding and evenly distributed functional groups such as –OH, –O–, and –F impart MXene with excellent mechanical rigidity and thermal stability, and they have shown great promise as nanofillers in polymer-based membranes for gas separation [22]. Thus, the rational design of MXene-based membranes has dramatically improved over the last few years. Many studies have assessed MXene-based MMMs for water purification and pervaporation compared with other 2D fillers; however, the use of MXene as a filler in natural/biogas separation applications is still in the infancy stage. Luo et al. have synthesized MXene/PEG MMMs

and revealed an ideal selectivity of 32.18 for CO<sub>2</sub>/N<sub>2</sub> and 27.84 for the CO<sub>2</sub>/CH<sub>4</sub> gases pair [23]. Guan et al. have used pre-structured MXene/Pebax MMMs and demonstrated a CO<sub>2</sub>/N<sub>2</sub> selectivity of 104.85 [18]. Similarly, Liu et al. have synthesized a Pebax-based membrane filled with 2D MXene nanosheets and displayed a separation performance with a CO<sub>2</sub> permeance of 21.6 GPU and a CO<sub>2</sub>/N<sub>2</sub> selectivity of 72.5 [24]. However, to the best of our knowledge, there are no reports on the use of MXene nanosheets as a filler to prepare cellulose triacetate based MMMs for gas separation.

Generally, the most critical factor influencing the success of MMMs is sufficient compatibility between the continuous (polymers) and disperse (filler) phases. Aside from adjusting the surface chemical configuration of the fillers to reduce the gaps between filler and polymer, proper adjustment of the shape and size of particles has also been demonstrated as an efficacious approach to circumventing nonselective defect formation and improving the gas permeation efficiency [25].

Several studies have been published on the effect of filler size on gas separation efficiency. Tantekin-Ersolmaz et al. discovered a decrease in gas permeability with larger-sized filler particles as compared to the fillers with relatively smaller particle size. Silicate-PDMS MMMs loading with different sizes of fillers were compared in the study. The observed results were presumed likely due to the large area and abundant filler-polymer interfaces that the gas molecules have to cross in these cases [26]. Coronas et al. have stated that, compared with nanosized particles (MCM-41), micron-size particles (MCM-48) could provide a lower external surface area and reduce aggregation, and as a consequence improve the dispersibility and interaction with the polymer and, thus, providing higher efficiency [27]. However, these two abovementioned results contradict each other. In another study, Hashemifaed et al. used halloysite nanotubes (HNTs) with large pore size as fillers and reported on different interfacial phases for MMMs, comprising five representative morphologies (i.e., ideal, void, rigidified, pore-blocking, and agglomeration combined with pore-blocking). After comparison with minor pore size fillers [28], they concluded that the type of filler (large or small pore size), as well as the filler particle size, was among the most influential factors determining the separation efficiency/performance of MMMs [29].

Meanwhile, only a handful of studies have focused on the effect of filler shape on the gas separation behavior of MMMs. Kaliaguine et al. have emphasized that the permeability and selectivity of various polymer matrixes for the separation of different gas pairs can also be improved by the shape selectivity and specific adsorption properties of zeolitic crystals, combined with the fluent processibility of the polymer matrix [30]. Suen et al. have compared the gas selectivity of polyether sulfone (PES)-based MMMs containing two different fillers with different shapes/sizes. They compared the efficiency of a lamellar Na-montmorillonite clay (mean length of 500 nm) and spherical TiO<sub>2</sub> particles (70 nm) and concluded that the spherical TiO<sub>2</sub> particles formed an ideal interface morphology, thus obtaining better gas separation performance than MMMs containing lamellar MMT sheets [31].

In this study, we first explore the effect of different MXene filler loadings on the physicochemical properties and, hence, gas separation performance of cellulose triacetate-based membranes. The gas separation efficiency of this 2D filler is simultaneously compared with that of 1D and 0D fillers to reveal guiding principles for future work in this field.

## 2. Materials and Methodology

### 2.1. Chemicals

Titanium dioxide (Degussa, 99.9% purity, Sigma-Aldrich, St. Louis, MI, USA), titanium dioxide nanoparticles (>99.5%, Sigma-Aldrich), Ti<sub>3</sub>AlC<sub>2</sub> MAX phase material (Jinzhou Haixin Metal Materials, China), hydrofluoric acid (HF, Sigma-Aldrich), cellulose triacetate (CTA, acetyl content 43–44%, Acros Organics), 1-methyl-2-pyrrolidinone (NMP, ACS reagent >99.0%, Sigma-Aldrich), sodium hydroxide (NaOH, 98.99% purity, Duksan Chemical), and Hydrochloric acid (HCL, ACS reagent >99.0%, Duksan Chemical) were mainly

used for the synthesis of fillers as well as membranes. All chemicals were used as received without any further purification. Similarly, single gases ( $\text{CO}_2$ ,  $\text{CH}_4$ ,  $\text{C}_3\text{H}_8$ ,  $\text{C}_3\text{H}_6$ , and  $\text{SF}_6$ ) with a purity of >99.95% (Linde Gas) were used as received.

### 2.2. Synthesis of Fillers $\text{Ti}_3\text{C}_2\text{T}_x$ MXene, $\text{TiO}_2$ Nanotubes, and $\text{TiO}_2$ Nanoparticles

Multi-layered  $\text{Ti}_3\text{C}_2\text{T}_x$  MXene was synthesized following the method previously reported by Chia et al. [32]. Briefly, 5.0 g of  $\text{Ti}_3\text{AlC}_2$  MAX phase material was mixed with 250 mL HF (40 wt.%) solution and continuously stirred under at room temperature for 7 days. Then, the sample was separated through repeated centrifugation and re-dispersion in water until a neutral pH value for the residual water was obtained. Subsequently, the sample was dried for 48 h in a vacuum oven set at 50 °C. Similarly, the  $\text{TiO}_2$  nanotubes were synthesized through a similar procedure, as explained in a previous work by Regmi et al. [33]. Commercially available  $\text{TiO}_2$  nanoparticles were used without any further modification.

### 2.3. Synthesis of MMMs

The MXene filler-based CTA MMM was prepared using the protocol of Regmi et al. [33]. Membranes with different concentrations of MXene fillers (1–5 wt.%) were prepared. In brief, firstly the calculated amount of MXene filler was mixed with NMP solvent (25 mL). The mixture was then sonicated for 30 min, and further stirred for 4 h. Then, 1.62 g of CTA polymer was added to the mixture and stirred overnight (24 h), maintaining an oil bath temperature of 70 °C. The mixture was then left undisturbed for about 4 h. The membrane was cast into a glass plate using an applicator (Elcometer 3580, Germany). The casted membrane was left in an ambient condition for 48 h. Further, the membrane was dried in a vacuum oven at 50 °C for 6 h to ensure complete evaporation of the solvent. Prepared membranes were labeled CM1, CM2, CM3, CM4, and CM5 for 1–5 wt.% filler concentration, respectively. An analogous protocol was used to synthesize other MMMs containing 0D and 1D fillers, and the respective samples are denoted by S-0D and S-1D throughout the manuscript.

### 2.4. Characterization

Fourier transform infrared spectroscopy (FTIR) spectra of the samples were recorded using an iS50R FTIR spectrometer (Thermo Scientific, USA) in the range of 4000–500  $\text{cm}^{-1}$ . Sixteen scans were accumulated with a resolution of 4  $\text{cm}^{-1}$  for each spectrum in absorption mode. The morphology of the MXene was investigated using scanning electron microscopy (SEM) with an FEG electron source (Tescan Lyra dual-beam microscope). Membrane morphology and elemental distribution were analyzed using SEM/TOF-SIMS (scanning electron microscopy/time-of-flight secondary ion mass spectroscopy; Tescan, Czech Republic). The primary ion source was a Ga liquid metal ion gun. The primary ion source beam energy used was 30 keV, with a current of nearly 10 nA for surface abrasion. All the membrane samples were coated with gold (Au) for surface conductivity. Scanning electron microscopy (SEM, Tescan Lyra, Czech Republic; 15 kV accelerating voltage, SE detector) was used to evaluate the cross-section morphology of prepared samples possessing 0D, 1D, and 2D fillers. This microscopy was connected to energy-dispersive spectroscopy (EDS, Oxford Aztec, 80  $\text{mm}^2$ , High Wycombe, United Kingdom) and was further used to analyze the distribution of fillers in the polymer matrix (especially Ti). Prior to analysis, membranes were first dipped into liquid nitrogen, fractured into small pieces, and coated with Au using sputter coating. Transmission electron microscopy (TEM, JEM-2200FS, JEOL, Japan) was used to image the morphology of the nanofillers. The images were taken at an accelerating voltage of 200 kV in TEM imaging mode. The static contact angle values of the as-synthesized membranes were measured using a fully automated optical tensiometer (Attension Theta Flex Auto 3, Biolin Scientific) at ambient conditions. The contact angles of the membranes were measured using the sessile drop method. The camera captured the drop profile image of water, and a fitting method was used to determine the value of

the contact angle. Each membrane was measured four times, and the maximum error was calculated as  $\pm 6^\circ$ . Surface topography analysis of the synthesized membranes was carried out using a 3D optical profilometer (NewView 9000, ZYGO, USA). X-ray diffraction (XRD) measurements were carried out on a second-generation D2 Phaser X-ray diffractometer (Bruker, Germany) with Cu-K $\alpha$  radiation ( $\lambda = 1.540$ ), Selected Bragg  $2\theta$  angular regions were measured from  $5$  to  $80^\circ$  in  $0.02^\circ$  increments at room temperature. Survey and high-resolution X-ray photoelectron spectroscopy (XPS) analyses of MXene nanofillers were conducted on ESCAProbeP Spectrometer (Omicron Nanotechnology Ltd., Germany), and the primary X-ray beam was monochrome radiation of an Al-K $\alpha$  source (1486.7 eV). Thermal stability was determined by thermogravimetric analysis (TGA; TG5500, TA instrument, USA) in an N<sub>2</sub> atmosphere (flow rate of 35 mLmin<sup>-1</sup>) from 25 to 800 °C at a scan rate of 10 °C min<sup>-1</sup>. Differential scanning calorimetry (DSC) (DSC3+, Mettler Toledo, Switzerland) was used for thermal analysis of the synthesized membranes. N<sub>2</sub> was used as a purge gas, with a flow rate of 30 mL min<sup>-1</sup>. Each sample was placed in an aluminum crucible, and scanning was performed with a temperature rate of 10 °C min<sup>-1</sup> from 25 to 400 °C.

### 2.5. Gas Sorption and Permeation Measurements

Gas sorption experiments were performed gravimetrically at 25 °C in a pressure range from 0.01 to 1.5 MPa, using a self-developed sorption apparatus equipped with a calibrator (McBain quartz spiral balance) [34]. An in-house designed sorption apparatus equipped with a calibrator (McBain quartz spiral balance) that gravimetrically evaluated the gas sorption efficiency of the prepared membrane materials was used. The absorption experiment was conducted at 25 °C in a pressure range from 0.01 to 1.5 MPa. Similarly, the gas permeation efficiency was determined using a tailor-made time lag permeation setup [35]. The experimental conditions and protocol for sorption and permeation were adapted from the previous work of Regmi et al. [33,36]. Membrane discs with an effective surface area of 2.14 cm<sup>2</sup> were placed in the membrane permeation cell. Before starting the gas permeation experiment, all the trapped air inside the cell was evacuated using a vacuum at both ends. In addition, the permeation cell was regularly evacuated with a vacuum pump to remove the trapped gases inside the cell prior to each gas sorption experiment. The permeation data were recorded using the SWeTr version 1.13 (2003 Neovision, Czech Republic) software until the steady-state permeation was reached. The pressures on both the feed and permeated sides were maintained at 1.5 bar. Three consecutive measurements were taken for every gas studied, and the average value was calculated. The maximum experimental error was estimated to be 8–10%.

The permeability ( $P_i$ ; 1 Barrer =  $10^{-10}$  cm<sup>3</sup> (STP) cm cm<sup>-2</sup> s<sup>-1</sup> cmHg<sup>-1</sup>) of a gas  $i$  is given by

$$P_i = D_i S_i \quad (1)$$

where  $D_i$  and  $S_i$  represent the diffusion and solubility coefficients of component  $i$ , respectively. Permeability was calculated by differentiating the pressure increase as a function of time, using the following equation:

$$P = \frac{V_d l}{P_2 A R T} \left[ \left( \frac{dp_1}{dt} \right)_{ss} - \left( \frac{dp_1}{dt} \right)_{leak} \right] \quad (2)$$

where  $V_d$  is a downstream volume (cm<sup>3</sup>),  $l$  is the membrane thickness (cm),  $P_2$  is the upstream absolute pressure (cmHg),  $A$  is the active surface area of the membrane (cm<sup>2</sup>),  $T$  is the temperature (K),  $R$  is the universal gas constant (cm<sup>3</sup> cmHg mol<sup>-1</sup> K<sup>-1</sup>),  $\left( \frac{dp_1}{dt} \right)_{ss}$  is the rate of downstream pressure rise during testing (cmHgs<sup>-1</sup>), and  $\left( \frac{dp_1}{dt} \right)_{leak}$  is the rate of downstream pressure rise under a vacuum (cmHgs<sup>-1</sup>).

The fluxes in the membrane module were kept constant during the experiments. The downstream pressure was raised linearly as a function of time, until a steady state was

reached. This time duration, the so-called time lag ( $\theta$ ), was used for the evaluation of the diffusion coefficient ( $D$ ) using the following equation:

$$D = \frac{l^2}{6\theta} \quad (3)$$

where  $l$  is the membrane thickness.

The ideal selectivity was calculated as a ratio of permeabilities of a pair of pure gases ( $x$  and  $y$ ) according to the following equation:

$$\alpha_{xy} = \frac{P_x}{P_y} \quad (4)$$

### 3. Results and Discussion

Among different MXene materials,  $\text{Ti}_3\text{C}_2\text{T}_x$  was taken as filler in the CTA polymer matrix to facilitate selective gas transport. XPS survey spectra of MXene (Figure S1, Supplementary Materials) revealed the presence of Ti, C, O, and F. The high-resolution XPS spectra for Ti, C, and O for  $\text{Ti}_3\text{C}_2\text{T}_x$  MXene and their respective peak fits are displayed in Figure 1. Ti2p peaks centered at 454.7 and 461.6 eV suggest the formation of Ti–C bonds [37], and the calculated  $\Delta\text{BE}$  of 6.9 eV between the Ti2p<sub>3/2</sub> (455.7 eV) and Ti2p<sub>1/2</sub> (462.3 eV) indicate the formation of  $\text{Ti}^{3+}$  species [38]. The C1s region deconvolutes into five different peaks at binding energies of 281.7, 285.3, 286.9, 288.9, and 289.8 eV. These peaks are assigned to Ti–C, C–C, C–O, OH–C=O, and C–F bonds, respectively [39]. Similarly, in O1s, the binding energies at 529.1, 530.0, 531.0, and 532.5 eV are related to O–Ti, C–Ti–O, C–Ti–(OH)<sub>x</sub>, and H–O–H bonds, respectively [40].

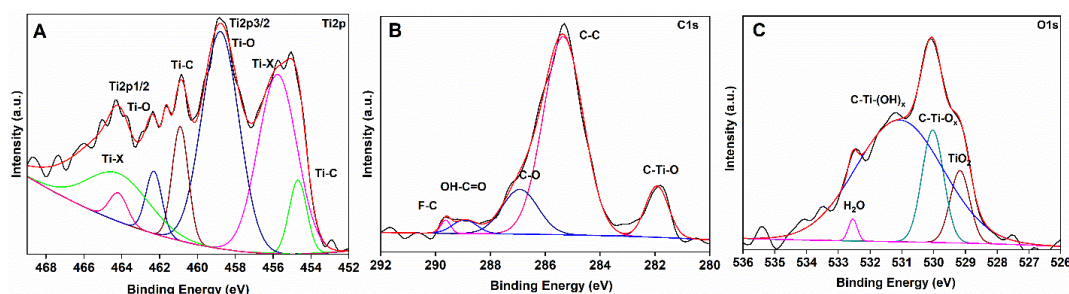


**Figure 1.** High resolution XPS spectra of; (A) Ti2p, (B) C1s and, (C) O1s for  $\text{Ti}_3\text{C}_2\text{T}_x$  MXene nanofiller.

Figure 2 shows the FTIR spectrum of pristine CTA membrane and MXene-incorporated CTA-based MMMs. The absorption band located around  $1741\text{ cm}^{-1}$  can be attributed to the stretching vibration of the C=O group. The absorption band at  $1370\text{ cm}^{-1}$  represents the  $\text{CH}_3$  acetyl group. Bands at  $1216$  and  $1037\text{ cm}^{-1}$  correspond to the stretching mode of C–O single bonds. The less intense band at  $2936\text{ cm}^{-1}$  is ascribed to the C–H bond [41,42]. Figure S2 represents the FTIR spectra of the pristine MXene nanosheet. The absorption peak at  $584\text{ cm}^{-1}$ , which corresponds to the –OH group, is evidence of typical –OH vibration [43]. Similarly, the absorption peak centered at  $650\text{ cm}^{-1}$  is assigned to the Ti–O group [38]. The absorption band at  $3725\text{ cm}^{-1}$  is due to the –OH functional group out-of-plane vibration of MXene [44]. No significant difference in FTIR spectra between pristine CTA and corresponding MMMs was observed, except for a decrease in the characteristic peak intensity of CTA in MMMs with an increase in the concentration of loaded MXene nanofillers. This behavior can be ascribed to the decreased polymer concentration due to the presence of fillers, as well as the interactions of the polymer matrix with the MXene [45]. Figure S3 presents the XRD spectra of as-prepared MMMs, the MXene nanoparticles, and pristine CTA membrane. The broad peak of pristine CTA that centered at  $19.5$   $2\theta$  degrees depict the semi-crystalline nature of the polymer. The appearance of diffraction peaks of both fillers and polymer in the diffraction patterns of MMMs confirms the homogeneous distribution

of MXene filler in the CTA matrix. Furthermore, the intensity of the MXene crystalline peaks intensifies with increased MXene loading concentration in MMMs, suggesting that the crystalline structure of MXene remains unchanged after being incorporated into the CTA matrix. Meanwhile, the broad peak of the polymer became relatively less noticeable.

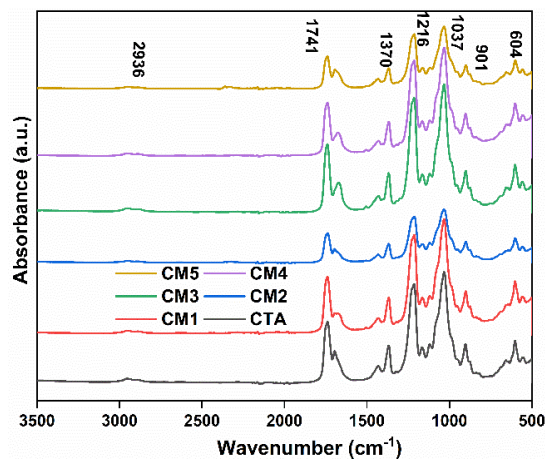


Figure 2. FTIR spectra of the synthesized MMM samples.

The surface properties of the fabricated membranes were found to be dependent on the amount of filler added. Figure 3 shows the surface morphology and cross-sections of the synthesized MMMs. The surface of each sample presents a fairly compact morphology, with ridges and valleys, and is free of defects such as pores and cracks. Cross-section images display a homogeneous phase, with solid and dense structure with defect-free morphology for all the synthesized membranes. No significant observable voids were seen at lower concentrations of the fillers. This indicates the excellent interfacial adhesion of the MXene surface with the CTA matrix. This further suggests the formation of hydrogen bonds between them. However, at a higher concentration, the aggregation of MXene results in increased sizes of void spaces between the polymer matrix and fillers, thus improving CO<sub>2</sub> and CH<sub>4</sub> permeability, which leads to deterioration of the gas separation selectivity.

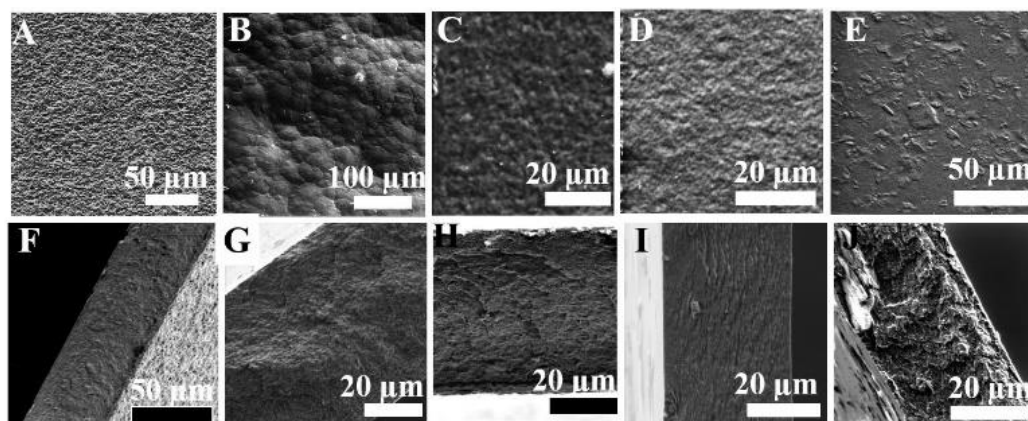
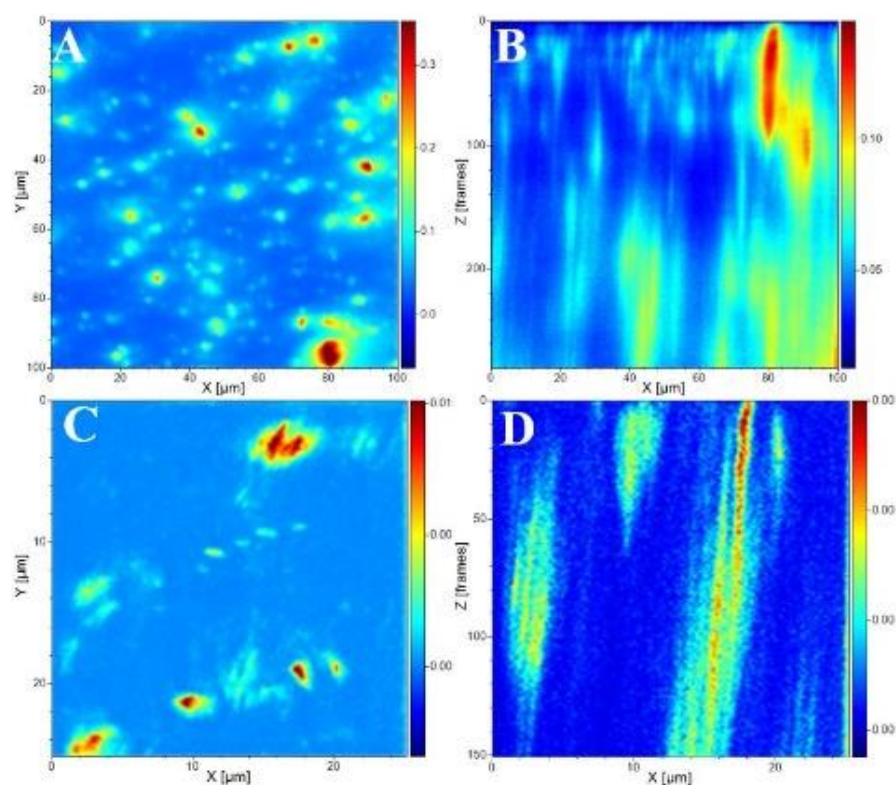


Figure 3. Surface and its corresponding cross-sectional morphologies of the prepared MMMs: (A,F) CM1; (B,G) CM2; (C,H) CM3; (D,I) CM4; and (E,J) CM5.

Furthermore, the topography of the prepared membranes was studied using a 3D profilometer, as shown in Figure S4. The surface roughness of the membranes increases with the filler concentration. The roughness follows the order of CM1 (Sq, 0.187  $\mu\text{m}$ ) < CM2 (Sq, 0.381  $\mu\text{m}$ ) < CM3 (Sq, 0.468  $\mu\text{m}$ ) < CM4 (Sq, 0.476  $\mu\text{m}$ ) < CM5 (Sq, 0.517  $\mu\text{m}$ ). It is presumed that, as the filler concentration increased, an increased amount of nanofillers bonded to the membrane surface increased, leading to high roughness. The water contact

angle of the synthesized membranes was also evaluated, and the results are displayed in Figure S5. A contact angle of  $53.3^\circ$  was reported for pristine CTA membrane in previous work [33]. The contact angles of all the synthesized MMMs were higher than that of the pristine membrane. The measured contact angle values for the synthesized samples are as follows: CM1,  $60.98^\circ$ ; CM2,  $64.82^\circ$ ; CM3,  $65.17^\circ$ ; CM4,  $71.82^\circ$ ; and CM5,  $69.48^\circ$ . With an increase in MXene loading, the water contact angle increases, indicating that the surface roughness is also increased.

Figure 4 shows filler distribution maps across the surface (top) and cross-section of the membrane sample CM3. The image reveals that the filler particles are homogeneously distributed throughout the membrane with few aggregations. This is further supported by the depth profile of the Ti element shown in Figure S6.



**Figure 4.** TOF-SIMS image of  $m/z$  (Ti element) distribution on (A) CM3 membrane sample surface and (B) the corresponding depth image, as well as (C,D) images corresponding to similar measurements along the membrane cross-section.

The thermal stability of the as-prepared MMMs at various MXene loading concentrations is depicted in Figure 5. TGA and its corresponding DTG spectra revealed two weight loss regions. The first region, at a temperature of  $152\text{--}195^\circ\text{C}$ , is characterized by weight loss of  $13.2 \pm 2\%$ , which was due to desorption of physically/chemically bound water, removal of trapped solvent, and dissociation of small amounts of esterified chains as well as acetylated cellulose [46]. The second transitional region, at around  $363 \pm 3^\circ\text{C}$ , shows a major decomposition range corresponding to a significant weight loss of  $85 \pm 3\%$ , which appears to be due to degradation of the main polymer chain. The decomposition of MMMs, compared with pristine CTA [47], starts at an elevated temperature due to the strong interactions between the polymer and filler through the polar groups, which decrease the thermal motion of the polymer; thus, the amount of energy required for polymer chain movement or segmentation is increased, leading to the enhanced thermal stability.

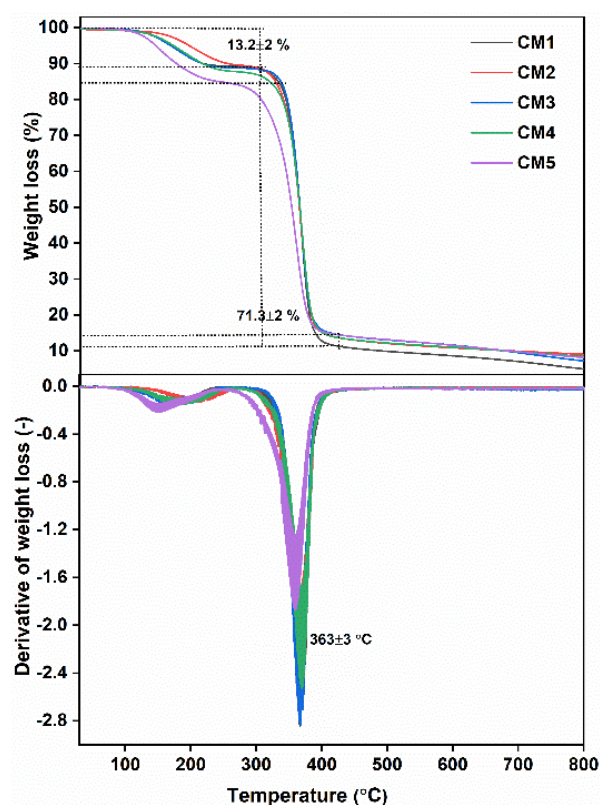


Figure 5. TGA DTG spectra of MMMs with different MXene filler loadings.

Similarly, the thermal behavior of membrane materials was further evaluated through DSC analysis. Figure 6 shows the DSC spectra of synthesized MMMs. The broad exothermic peak centered at 138.2 °C corresponds to the crystallization temperature. Compared with pristine CTA (with a crystallization temperature of 156 °C) [42], the crystallization peak shifted toward the lower temperature side with an increase in filler concentration. Furthermore, the observed broader and lower-intensity peak of the MMMs as compared to pristine CTA is ascribed to the slow crystallization. The addition of MXene fillers possessing polar groups should facilitate coordination with the polymer chains, thus reducing its tendency to form crystalline phases [48]. Similarly, the endothermic peak corresponding to fusion/melting emerges at a temperature of 298.5 °C, higher than for pristine CTA (melting/fusion temperature 289 °C) [47]. These results can be attributed to the excellent interaction and distribution of the filler particles within the polymer matrix.

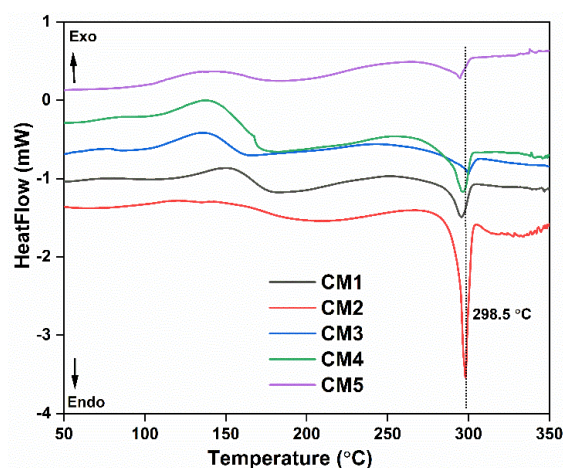
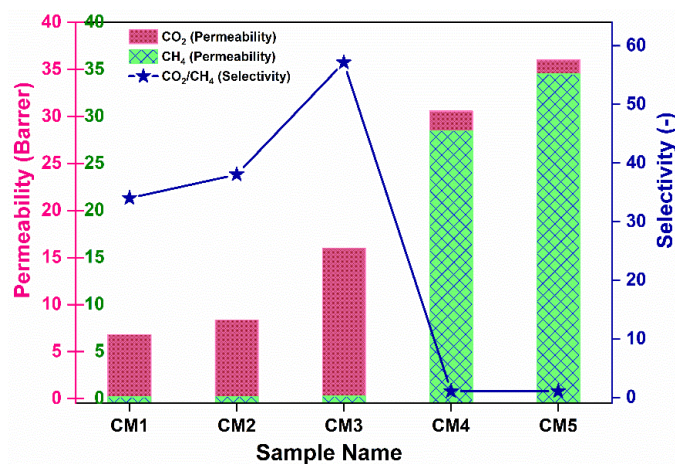


Figure 6. DSC thermogram of the MMMs synthesized with various filler loadings.

#### 4. Gas Separation Performances Evaluation

To study the CO<sub>2</sub> and CH<sub>4</sub> gas transport efficiency of the CTA-based membranes, permeation evaluation was performed in a variable volume-constant pressure custom-built time lag permeation setup. The experiment was operated at 25 °C temperature and 1.5 bar feed pressure. A simple soap film flowmeter was used to obtain the flow rate, which was measured using a soap film flow meter. First, we investigated the effect of MXene concentration on the CO<sub>2</sub>/CH<sub>4</sub> separation performance. As shown in Figure 7, the pure gas (CO<sub>2</sub> and CH<sub>4</sub>) gradually increased with MXene loading up to 5 wt.%, with the CO<sub>2</sub> as well as CH<sub>4</sub> permeance increasing. Compared to the increase in CH<sub>4</sub> permeance up to 3 wt.%, a dramatic increase in CH<sub>4</sub> permeance was observed at higher MXene loadings. Hence, the CO<sub>2</sub>/CH<sub>4</sub> selectivity increases up to 3 wt.% (reaching 57.14) and then decreases to 5 wt.%. Compared with the CO<sub>2</sub> permeance of pristine CTA (3.01 Barrer) [47], the permeability of the 3 wt.% MXene-containing CTA sample is increased 5-fold, reaching a permeability of 16 Barrer, with a 2-fold increase in CO<sub>2</sub>/CH<sub>4</sub> selectivity. Thus, introducing MXene nanosheets (up to 3 wt.%) provides additional molecular transport channels, enhancing CO<sub>2</sub> permeance and CO<sub>2</sub>/CH<sub>4</sub> selectivity. The enhancement in gas separation performance is also attributed to the high CO<sub>2</sub> absorption capacity (Figure S7), due to the presence of abundant polar groups on the MXene surface as well as the assembly of the laminar structure with nanochannels that enhance the diffusion of gas molecules (Figure S8), thus increasing the permeability. Hence, it can be concluded that a solution–diffusion transport mechanism was obeyed. The further decrease in selectivity at a higher loading of MXene above 3 wt.% can be attributed to the generation of non-selective regions due to the accumulation of filler nanoparticles [23].



**Figure 7.** Single gas separation behavior of synthesized MMMs at various concentration of Mxene nanofillers.

Figure 8 compares the CO<sub>2</sub>/CH<sub>4</sub> permeation efficiency of the synthesized MMMs in this work with the standard Robeson's 2008 upper bound plot. It is observed that, with an increase in the concentration of MXene as a nanofiller, the permeance and selectivity increase up to 3 wt.%, almost reaching the upper bound, before decreasing in selectivity as the concentration is further increased. The increase in selectivity can be attributed to the high affinity of the fillers for CO<sub>2</sub>.

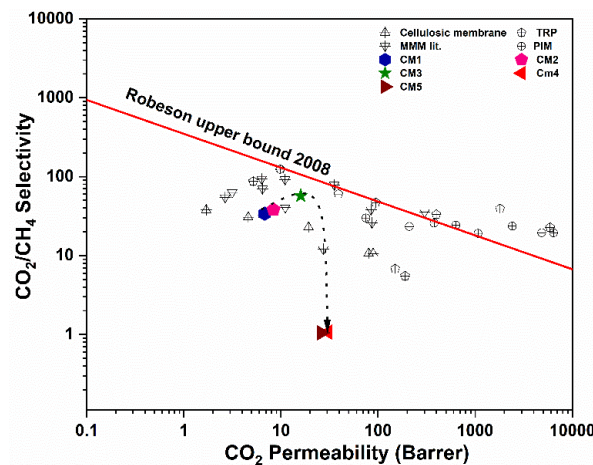
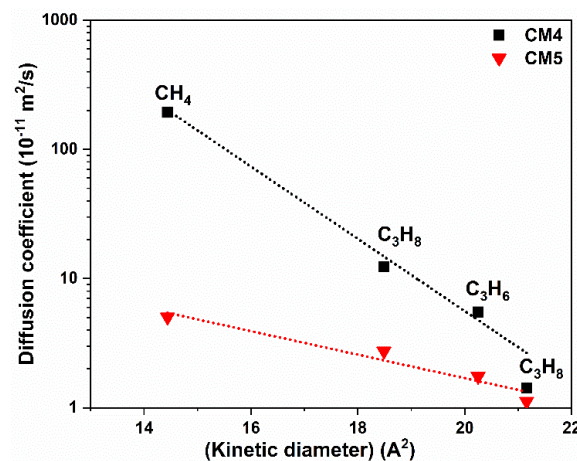


**Figure 8.** Comparison of CO<sub>2</sub>/CH<sub>4</sub> separation performance of the as-synthesized membranes, possessing different concentration of MXene filler, with the standard Robeson’s 2008 upper bound plot [49,50]. The dashed arrow serves to guide the eye. Some of the values in the data point are adapted with permission from ref. [49].

To further evaluate the drastic change in the permeability and selectivity trend of the MMMs at MXene concentrations higher than 3 wt.%, we measured the permeability of different hydrocarbons such as propane (C<sub>3</sub>H<sub>8</sub>), propylene (C<sub>3</sub>H<sub>6</sub>), butane (C<sub>4</sub>H<sub>10</sub>), and sulfur hexafluoride (SF<sub>6</sub>) through the CM<sub>4</sub> and CM<sub>5</sub> membranes. The results are provided in Figure S9. The order of gas permeability for both membranes is P<sub>CH<sub>4</sub></sub> > P<sub>C<sub>3</sub>H<sub>8</sub></sub> > P<sub>C<sub>3</sub>H<sub>6</sub></sub> > P<sub>C<sub>4</sub>H<sub>10</sub></sub> > P<sub>SF<sub>6</sub></sub>, which corresponds to the kinetic diameters of the studied gases. In principle, the permeation of gas molecules in polymeric membranes occurs by a solution–diffusion process. However, for membranes with a higher concentration of MXene as a filler (above 4 wt.%), gas separation efficiency is controlled by a diffusion mechanism, which can be ascribed as molecular sieving. Generally, for small and almost spherical gas molecules, the logarithm of diffusion coefficient (*D*) is proportional to the square of the molecular kinetic diameter (*d*), as shown in the equation [51]:

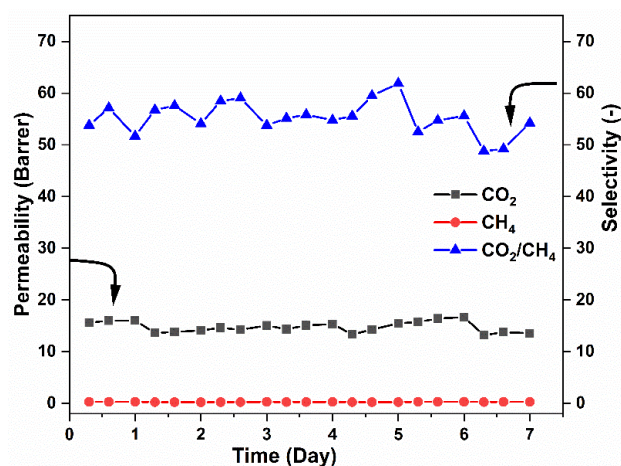
$$\log(D) \propto d^2 \tag{5}$$

Figure 9 shows the relation of log (*D*) and *d*<sup>2</sup> for the different hydrocarbons. It is observed that this correlation, which states that the diffusion coefficient decreases with the molecular size, is obeyed by the gases in the study.



**Figure 9.** Relation between the diffusion coefficient and the corresponding kinetic diameter of the different hydrocarbons.

Additionally, the CO<sub>2</sub>/CH<sub>4</sub> separation efficiency of MXene-CTA MMMs was studied through a one-week-long separation experiment at 1.5 bar pressure and 25 °C temperature. At least three consecutive measurements were performed each day. The deviation in the permeability was calculated to be below 10%. As shown in Figure 10, the permeability and selectivity of the membrane sample (CM3) for CO<sub>2</sub>/CH<sub>4</sub> separation remained nearly the same at the beginning as after the one-week experiment. This result thus suggests the high stability of the synthesized MMM samples and their practical potential in separation of CO<sub>2</sub> from bio/natural gas.



**Figure 10.** Long-term stability test on CM3 sample for CO<sub>2</sub> and CH<sub>4</sub> single-gas separation.

To analyze the impact of the filler shape on the gas separation performance, membranes with different fillers—namely, 0D (TiO<sub>2</sub> nanosphere) and 1D (TiO<sub>2</sub> nanotube) fillers—were synthesized, and their gas (CO<sub>2</sub> and CH<sub>4</sub>) separation efficiency was compared with that of a membrane containing 2D (MXene nanosheet) filler.

TEM, as well as SEM, was used to evaluate the morphology of the as-synthesized fillers (Figure 11). The TEM image in Figure 11A shows uniform TiO<sub>2</sub> nanospheres (0D) with an average particle size of 20 nm. Figure 11B demonstrates the thin fiber-like hollow tubular structure of the TiO<sub>2</sub> nanotubes (1D). Figure 11C, D show the TEM and SEM images of MXene sheets (2D), with large lateral dimensions and rigid sheets that are stacked in an orderly manner, naturally generating interlayer channels through direct self-stacking. Figure 11E–G display the membrane morphology and pattern of the fillers distributed throughout the membrane. The filler particles were homogeneously distributed throughout the membrane with only a few aggregations, as revealed through elemental mapping. Different membrane morphologies can be obtained by adding fillers of different shapes. Upon addition of 0D and 1D fillers, voids ranging from nm- to μm-scale can be observed, thus improving gas permeability. In contrast, in the case of 2D fillers, a highly compact dense morphology free of voids is observed.

The efficiencies of different filler loaded MMMs towards gas permeability and selectivity are presented in Figure 12. The CO<sub>2</sub> permeability and CO<sub>2</sub>/CH<sub>4</sub> selectivity correspond to the following order: 2D > 1D > 0D. The use of 0D fillers (S-0D) marginally increases the permeability of CO<sub>2</sub> and CO<sub>2</sub>/CH<sub>4</sub> selectivity compared with pristine CTA polymer, as has been evidenced in our previous work [47]. Such increased selectivity is attributed to the availability of hydroxyl groups on the TiO<sub>2</sub> surface that have stronger interactions with polar CO<sub>2</sub> molecules as compared to non-polar CH<sub>4</sub> molecules, thus promoting increased selectivity. For sample S-1D, permeability of both the CO<sub>2</sub> and CH<sub>4</sub> gases increased, while a marginal increase in CO<sub>2</sub>/CH<sub>4</sub> selectivity was observed. The hollow structure of vertically aligned TNTs can serve as rapid transport channels that function as less-restricted gas diffusional pathways with minimal permeation barrier, thus increasing the permeability of CO<sub>2</sub> and CH<sub>4</sub> [33]. However, partial blockage of the tubes by polymer chains is inevitable. It is speculated that embedding 1D fillers provides a tortuous network of diffusion paths

for the large molecules such as  $\text{CH}_4$  through the membrane. In the meantime, such a network might not be adequate to moderate the diffusion of smaller molecules, such as  $\text{CO}_2$ . Likewise, due to the insufficient interaction between TNT fillers and polymer phase, undesirable channels might be formed at the interfacial region between polymer and fillers, further enabling the transport of  $\text{CH}_4$ . The enhanced gas selectivity of membrane S-2D containing 2D filler was ascribed to the preferential horizontal orientation of the sheets, which hinders the transport of larger gas molecules ( $\text{CH}_4$ ). Similarly, the functional polar groups on the surface can form partial bonds with  $\text{CO}_2$ , thus providing a facilitated transport mechanism. Apart from the significant concerns of nanoparticle structures, nanoparticle shapes cannot be avoided when matrix–filler interactions are considered a significant drawback in polymer nanocomposites. The adjustment of nanofiller shapes will automatically lead to variations in the contact areas between polymer matrices and fillers, which effectively determines the volume of the interfacial regions [52] and, thus, ultimately affects gas permeability and selectivity. Further research utilizing molecular simulation is essential, which is expected to further extend knowledge in this area.

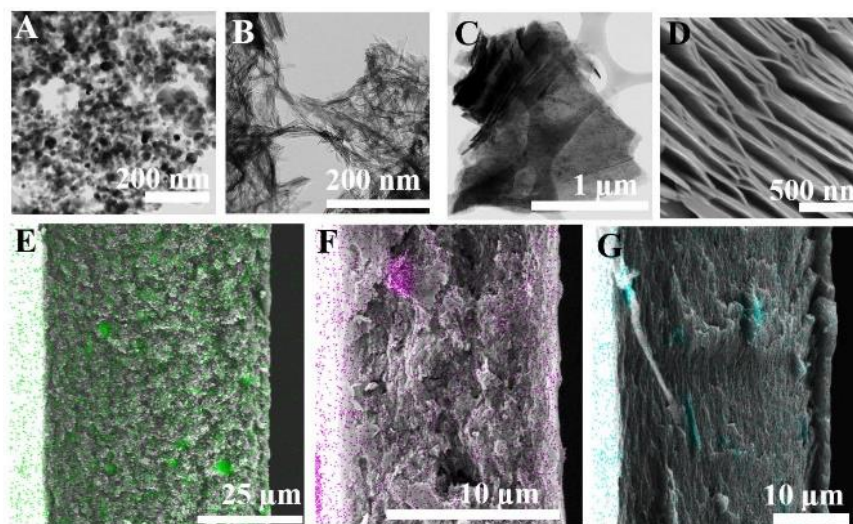


**Figure 11.** TEM images (A–C) of the 0D, 1D, and 2D nanofillers; SEM image (D) of the 2D nanofiller; and SEM-EDS images of cross-sections of (E) 0D, (F) 1D, and (G) 2D filler-incorporated MMMs overlaid with the distributed corresponding Ti element (colored).

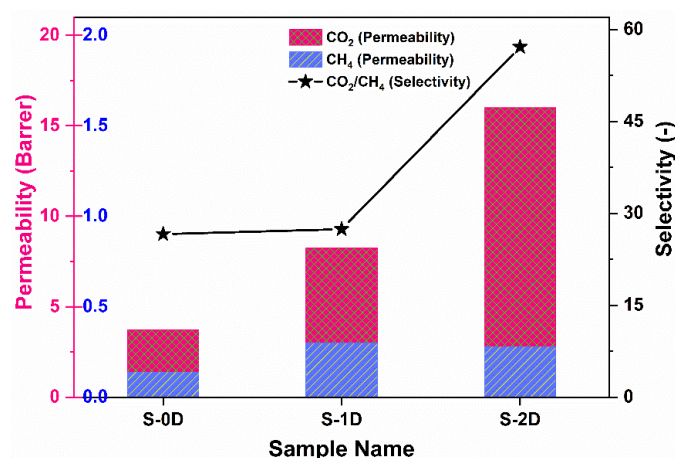


**Figure 12.** Comparison of gas separation efficiency of MMMs synthesized using 0D, 1D, and 2D fillers.

## 5. Conclusions

In summary, we first synthesized a series of CTA-based MMMs with different concentrations of MXene fillers and assessed their performance in  $\text{CO}_2/\text{CH}_4$  separation. The

sample containing 3 wt.% of embedded MXene exhibited the best separation performance, with a CO<sub>2</sub> permeability of 16 barrer and ideal CO<sub>2</sub>/CH<sub>4</sub> selectivity of 57.14. Among the fillers with different shapes (i.e., 0D, 1D, and 2D), the 2D fillers (MXene) stand out as a promising candidate for the preparation of MMMs due to their superior interfacial compatibility with polymer matrix, as depicted by the dense, compact, and homogeneous morphology free of voids as observed by SEM. Additional advantageous features include the presence of abundant polar groups and the lamellar nanosheet arrangement, which provide an additional nanochannel for gas transport with the two-fold enhancement of CO<sub>2</sub>/CH<sub>4</sub> separation compared with the pristine CTA membrane. The high thermal performance and long-term operational stability of the designed materials represent a new milestone for MMMs as alternatives for applications in challenging natural gas purification applications. This work thus provides insight into the development of MMMs with high performance in gas separation toward overcoming current bottlenecks in this area.

**Supplementary Materials:** The following supporting information can be downloaded at: <https://www.mdpi.com/article/10.3390/membranes12100917/s1>, Figure S1: XPS survey spectrum of MXene nanosheets, Figure S2: FTIR of MXene nanosheets, Figure S3: XRD patterns of synthesized MMMs with different loading concentrations of MXene., Figure S4: Surface topography analysis of the prepared MMMs containing different loading concentrations of MXene filler., Figure S5: Water contact angle evaluation of MMMs synthesized with different MXene loading concentrations., Figure S6: Depth profile analysis of Ti element distribution in CM3 sample; A) Surface and, B) cross-section., Figure S7: CO<sub>2</sub> uptake comparison between pristine polymer and MMM with MXene filler., Figure S8: Diffusion coefficient as a function of MXene fillers concentration., and Figure S9: Permeability comparison of different hydrocarbon and SF<sub>6</sub> via CM4 and CM3 membranes.

**Author Contributions:** C.R. designed the project, performed the experiment, analyzed data, and wrote the manuscript. J.A. synthesized the MXenes and revised the manuscript. V.M. analyzed the membrane morphology and elemental distribution via SEM/TOF-SIMS and revised the manuscript. Z.S. provided the laboratory facilities for the synthesis of membrane materials, provided access to different analytical tools for studying membrane properties, and revised the manuscript. S.A. assisted in gas separation measurements and surface topography analysis and revised the manuscript. K.F. conceptualized and revised the manuscript. All authors have read and agreed to the published version of the manuscript.

**Funding:** This research was financially supported by the European Structural and Investment Funds OP RDE-funded project ‘ChemJets2’ (CZ.02.2.69/0.0/0.0/18-053/ 0016974) and partly by the project of the Czech Ministry of Education, Youth and Sports (LTAUSA 19038).

**Institutional Review Board Statement:** Not applicable.

**Informed Consent Statement:** Not applicable.

**Data Availability Statement:** Not applicable.

**Acknowledgments:** The authors acknowledge Ivo Marek, Sajdl Petr, and Ing. Jakub Havlín, Laboratory of Transmission Electron Microscopy, Laboratory of Surface Analysis and Thermal-Gravimetric Analysis under the Central Laboratory of UCT Prague, for TEM, XPS, and TGA measurements, respectively; Filip Prusa for his contribution to the SEM and EDS measurements; and Alena Randova for water contact angle measurements. C.R. acknowledges the European Structural and Investment Funds OP RDE-funded project ‘ChemJets2’ (CZ.02.2.69/0.0/0.0/18-053/ 0016974). J.A. also acknowledges the European Structural and Investment Funds, OPRDE-funded project: “CHEMFELL IV” (No. CZ.02.2.69/0.0/0.0/20-079/0017899).

**Conflicts of Interest:** The authors declare no conflict of interest.

## References

1. Li, J.; Li, X.; van der Bruggen, B. An MXene-based membrane for molecular separation. *Environ. Sci. Nano* **2020**, *7*, 1289–1304. [[CrossRef](#)]
2. Cheng, Y.; Pu, Y.; Zhao, D. Two-dimensional membranes: New paradigms for high-performance separation membranes. *Chem.—Asian J.* **2020**, *15*, 2241–2270. [[CrossRef](#)] [[PubMed](#)]

3. Robeson, L.M. Correlation of separation factor versus permeability for polymeric membranes. *J. Membr. Sci.* **1991**, *62*, 165–185. [[CrossRef](#)]
4. Shi, F.; Sun, J.; Wang, J.; Liu, M.; Yan, Z.; Zhu, B.; Li, Y.; Cao, X. MXene versus graphene oxide: Investigation on the effects of 2D nanosheets in mixed matrix membranes for CO<sub>2</sub> separation. *J. Membr. Sci.* **2021**, *620*, 118850. [[CrossRef](#)]
5. Carreon, M.A. *Membranes for Gas Separations*; World Scientific Publishing Company: Singapore, 2017.
6. Goh, P.S.; Ismail, A.F.; Sanip, S.M.; Ng, B.C.; Aziz, M. Recent advances of inorganic fillers in mixed matrix membrane for gas separation. *Sep. Purif. Technol.* **2011**, *81*, 243–264. [[CrossRef](#)]
7. Ebert, K.; Fritsch, D.; Koll, J.; Tjahjajawiguna, C. Influence of inorganic fillers on the compaction behaviour of porous polymer-based membranes. *J. Membr. Sci.* **2004**, *233*, 71–78. [[CrossRef](#)]
8. Khraisheh, M.; Elhenawy, S.; AlMomani, F.; Al-Ghouti, M.; Hassan, M.K.; Hameed, B.H. Recent progress on nanomaterial-based membranes for water treatment. *Membranes* **2021**, *11*, 995. [[CrossRef](#)]
9. Ng, L.Y.; Mohammad, A.W.; Leo, C.P.; Hilal, N. Polymeric membranes incorporated with metal/metal oxide nanoparticles: A comprehensive review. *Desalination* **2013**, *308*, 15–33. [[CrossRef](#)]
10. Rezakazemi, M.; Amooghin, A.E.; Montazer-Rahmati, M.M.; Ismail, A.F.; Matsuura, T. State-of-the-art membrane-based CO<sub>2</sub> separation using mixed matrix membranes (MMMs): An overview on current status and future directions. *Prog. Polym. Sci.* **2014**, *39*, 817–861. [[CrossRef](#)]
11. Bernardo, P.; Drioli, E.; Golemme, G. Membrane gas separation: A review/state of the art. *Ind. Eng. Chem. Res.* **2009**, *48*, 4638–4663. [[CrossRef](#)]
12. Kamble, A.R.; Patel, C.M.; Murthy, Z.V.P. A review on the recent advances in mixed matrix membranes for gas separation processes. *Renew. Sustain. Energy Rev.* **2021**, *145*, 111062. [[CrossRef](#)]
13. Basu, S.; Cano-Odena, A.; Vankelecom, I.F.J. MOF-containing mixed-matrix membranes for CO<sub>2</sub>/CH<sub>4</sub> and CO<sub>2</sub>/N<sub>2</sub> binary gas mixture separations. *Sep. Purif. Technol.* **2011**, *81*, 31–40. [[CrossRef](#)]
14. Liu, X.; Ma, T.; Pinna, N.; Zhang, J. Two-dimensional nanostructured materials for gas sensing. *Adv. Funct. Mater.* **2017**, *27*, 1702168. [[CrossRef](#)]
15. Zhang, H. Ultrathin two-dimensional nanomaterials. *ACS Nano* **2015**, *9*, 9451–9469. [[CrossRef](#)] [[PubMed](#)]
16. Chen, D.; Zhu, H.; Liu, T. In situ thermal preparation of polyimide nanocomposite films containing functionalized graphene sheets. *ACS Appl. Mater. Interfaces* **2010**, *2*, 3702–3708. [[CrossRef](#)]
17. Compton, O.C.; Kim, S.; Pierre, C.; Torkelson, J.M.; Nguyen, S.T. Crumpled graphene nanosheets as highly effective barrier property enhancers. *Adv. Mater.* **2010**, *22*, 4759–4763. [[CrossRef](#)]
18. Guan, W.; Yang, X.; Dong, C.; Yan, X.; Zheng, W.; Xi, Y.; Ruan, X.; Dai, Y.; He, G. Prestructured MXene fillers with uniform channels to enhance CO<sub>2</sub> selective permeation in mixed matrix membranes. *J. Appl. Polym. Sci.* **2021**, *138*, 49895. [[CrossRef](#)]
19. Feijani, E.A.; Tavassoli, A.; Mahdavi, H.; Molavi, H. Effective gas separation through graphene oxide containing mixed matrix membranes. *J. Appl. Polym. Sci.* **2018**, *135*, 46271. [[CrossRef](#)]
20. Liu, Y.-C.; Chen, C.-Y.; Lin, G.-S.; Chen, C.-H.; Wu, K.C.W.; Lin, C.-H.; Tung, K.-L. Characterization and molecular simulation of Pebax-1657-based mixed matrix membranes incorporating MoS<sub>2</sub> nanosheets for carbon dioxide capture enhancement. *J. Membr. Sci.* **2019**, *582*, 358–366. [[CrossRef](#)]
21. Ren, C.E.; Hatzell, K.B.; Alhabeib, M.; Ling, Z.; Mahmoud, K.A.; Gogotsi, Y. Charge- and size-selective Ion sieving through Ti<sub>3</sub>C<sub>2</sub>T<sub>x</sub> MXene membranes. *J. Phys. Chem. Lett.* **2015**, *6*, 4026–4031. [[CrossRef](#)]
22. Yang, G.; Xie, Z.; Thornton, A.W.; Doherty, C.M.; Ding, M.; Xu, H.; Cran, M.; Ng, D.; Gray, S. Ultrathin poly (vinyl alcohol)/MXene nanofilm composite membrane with facile intrusion-free construction for pervaporative separations. *J. Membr. Sci.* **2020**, *614*, 118490.
23. Luo, W.; Niu, Z.; Mu, P.; Li, J. MXene/poly(ethylene glycol) mixed matrix membranes with excellent permeance for highly efficient separation of CO<sub>2</sub>/N<sub>2</sub> and CO<sub>2</sub>/CH<sub>4</sub>. *Colloids Surf. A Physicochem. Eng. Asp.* **2022**, *640*, 128481. [[CrossRef](#)]
24. Liu, G.; Cheng, L.; Chen, G.; Liang, F.; Liu, G.; Jin, W. Pebax-based membrane filled with two-dimensional Mxene nanosheets for efficient CO<sub>2</sub> capture. *Chem. Asian J.* **2020**, *15*, 2364–2370. [[PubMed](#)]
25. Aroon, M.A.; Ismail, A.F.; Matsuura, T.; Montazer-Rahmati, M.M. Performance studies of mixed matrix membranes for gas separation: A review. *Sep. Purif. Technol.* **2010**, *75*, 229–242.
26. Tantekin-Ersolmaz, Ş.B.; Atalay-Oral, Ç.; Tatlier, M.; Erdem-Şenatarlar, A.; Schoeman, B.; Sterte, J. Effect of zeolite particle size on the performance of polymer-zeolite mixed matrix membranes. *J. Membr. Sci.* **2000**, *175*, 285–288.
27. Zornoza, B.; Irusta, S.; Téllez, C.; Coronas, J. Mesoporous silica sphere-polysulfone mixed matrix membranes for gas separation. *Langmuir* **2009**, *25*, 5903–5909. [[CrossRef](#)]
28. Moore, T.T.; Koros, W.J. Non-ideal effects in organic-inorganic materials for gas separation membranes. *J. Mol. Struct.* **2005**, *739*, 87–98.
29. Hashemifard, S.A.; Ismail, A.F.; Matsuura, T. Mixed matrix membrane incorporated with large pore size halloysite nanotubes (HNTs) as filler for gas separation: Morphological diagram. *Chem. Eng. J.* **2011**, *172*, 581–590. [[CrossRef](#)]
30. Vinh-Thang, H.; Kaliaguine, S. Predictive models for mixed-matrix membrane performance: A review. *Chem. Rev.* **2013**, *113*, 4980–5028. [[CrossRef](#)]

31. Liang, C.-Y.; Uchytíl, P.; Petrychkovych, R.; Lai, Y.-C.; Friess, K.; Sipek, M.; Reddy, M.M.; Suen, S.-Y. A comparison on gas separation between PES (polyethersulfone)/MMT (Na-montmorillonite) and PES/TiO<sub>2</sub> mixed matrix membranes. *Sep. Purif. Technol.* **2012**, *92*, 57–63. [[CrossRef](#)]
32. Chia, H.L.; Mayorga-Martinez, C.C.; Antonatos, N.; Sofer, Z.; Gonzalez-Julian, J.J.; Webster, R.D.; Pumera, M. MXene Titanium carbide-based biosensor: Strong dependence of exfoliation method on performance. *Anal. Chem.* **2020**, *92*, 2452–2459. [[CrossRef](#)] [[PubMed](#)]
33. Regmi, C.; Ashtiani, S.; Průša, F.; Friess, K. Synergistic effect of hybridized TNT@GO fillers in CTA-based mixed matrix membranes for selective CO<sub>2</sub>/CH<sub>4</sub> separation. *Sep. Purif. Technol.* **2022**, *282*, 120128. [[CrossRef](#)]
34. Vopička, O.; Friess, K.; Hýnek, V.; Sysel, P.; Zgažar, M.; Šípek, M.; Pilnáček, K.; Lanč, M.; Jansen, J.C.; Mason, C.R.; et al. Equilibrium and transient sorption of vapours and gases in the polymer of intrinsic microporosity PIM-1. *J. Membr. Sci.* **2013**, *434*, 148–160. [[CrossRef](#)]
35. Friess, K.; Lanč, M.; Pilnáček, K.; Fíla, V.; Vopička, O.; Sedláková, Z.; Cowan, M.G.; McDanel, W.M.; Noble, R.D.; Gin, D.L.; et al. CO<sub>2</sub>/CH<sub>4</sub> separation performance of ionic-liquid-based epoxy-amine ion gel membranes under mixed feed conditions relevant to biogas processing. *J. Membr. Sci.* **2017**, *528*, 64–71. [[CrossRef](#)]
36. Regmi, C.; Ashtiani, S.; Sofer, Z.; Friess, K. Improved CO<sub>2</sub>/CH<sub>4</sub> separation properties of cellulose triacetate mixed-matrix membranes with CeO<sub>2</sub>@GO hybrid fillers. *Membranes* **2021**, *11*, 777. [[CrossRef](#)]
37. Gong, Y.; Tu, R.; Goto, T. High-speed deposition of titanium carbide coatings by laser-assisted metal-organic CVD. *Mater. Res. Bull.* **2013**, *48*, 2766–2770. [[CrossRef](#)]
38. Nawaz, R.; Kait, C.F.; Chia, H.Y.; Isa, M.H.; Huei, L.W. Glycerol-mediated facile synthesis of colored titania nanoparticles for visible light photodegradation of phenolic compounds. *Nanomaterials* **2019**, *9*, 1586. [[CrossRef](#)] [[PubMed](#)]
39. Zhao, J.; Zhang, L.; Xie, X.-Y.; Li, X.; Ma, Y.; Liu, Q.; Fang, W.-H.; Shi, X.; Cui, G.; Sun, X. Ti<sub>3</sub>C<sub>2</sub>T<sub>x</sub> (T = F, OH) MXene nanosheets: Conductive 2D catalysts for ambient electrohydrogenation of N<sub>2</sub> to NH<sub>3</sub>. *J. Mater. Chem. A* **2018**, *6*, 24031–24035.
40. Fu, Q.; Wen, J.; Zhang, N.; Wu, L.; Zhang, M.; Lin, S.; Gao, H.; Zhang, X. Free-standing Ti<sub>3</sub>C<sub>2</sub>T<sub>x</sub> electrode with ultrahigh volumetric capacitance. *RSC Adv.* **2017**, *7*, 11998–12005.
41. Amara, M.; Arous, O.; Smail, F.; Kerdjoudj, H.; Trari, M.; Bouguelia, A. An assembled poly-4-vinyl pyridine and cellulose triacetate membrane and Bi<sub>2</sub>S<sub>3</sub> electrode for photoelectrochemical diffusion of metallic ions. *J. Hazard. Mater.* **2009**, *169*, 195–202. [[CrossRef](#)]
42. Regmi, C.; Ashtiani, S.; Hrdlička, Z.; Friess, K. CO<sub>2</sub>/CH<sub>4</sub> and H<sub>2</sub>/CH<sub>4</sub> gas separation performance of CTA-TNT@CNT hybrid mixed matrix membranes. *Membranes* **2021**, *11*, 862. [[CrossRef](#)] [[PubMed](#)]
43. Qian, A.; Seo, J.Y.; Shi, H.; Lee, J.Y.; Chung, C.-H. Surface functional groups and electrochemical behavior in dimethyl sulfoxide-delaminated Ti<sub>3</sub>C<sub>2</sub>T<sub>x</sub> MXene. *ChemSusChem* **2018**, *11*, 3719–3723. [[CrossRef](#)]
44. Satheeshkumar, E.; Makaryan, T.; Melikyan, A.; Minassian, H.; Gogotsi, Y.; Yoshimura, M. One-step Solution Processing of Ag, Au and Pd@MXene Hybrids for SERS. *Sci. Rep.* **2016**, *6*, 32049. [[CrossRef](#)]
45. Zhuang, G.-L.; Tseng, H.-H.; Wey, M.-Y. Preparation of PPO-silica mixed matrix membranes by in-situ sol-gel method for H<sub>2</sub>/CO<sub>2</sub> separation. *Int. J. Hydrog. Energy* **2014**, *39*, 17178–17190. [[CrossRef](#)]
46. Nabili, A.; Fattoum, A.; Brochier-Salon, M.-C.; Bras, J.; Elaloui, E. Synthesis of cellulose triacetate-I from microfibrillated date seeds cellulose (*Phoenix dactylifera* L.). *Iran. Polym. J.* **2017**, *26*, 137–147. [[CrossRef](#)]
47. Regmi, C.; Ashtiani, S.; Sofer, Z.; Hrdlička, Z.; Průša, F.; Vopička, O.; Friess, K. CeO<sub>2</sub>-blended cellulose triacetate mixed-matrix membranes for selective CO<sub>2</sub> separation. *Membranes* **2021**, *11*, 632. [[CrossRef](#)] [[PubMed](#)]
48. Chen, S.; Xie, S.; Guang, S.; Bao, J.; Zhang, X.; Chen, W. Crystallization and thermal behaviors of poly(ethylene terephthalate)/bisphenols complexes through melt post-polycondensation. *Polymers* **2020**, *12*, 3053. [[CrossRef](#)] [[PubMed](#)]
49. Robeson, L.M. The upper bound revisited. *J. Membr. Sci.* **2008**, *320*, 390–400. [[CrossRef](#)]
50. Comesaña-Gándara, B.; Chen, J.; Bezzu, C.G.; Carta, M.; Rose, I.; Ferrari, M.-C.; Esposito, E.; Fuoco, A.; Jansen, J.C.; McKeown, N.B. Redefining the Robeson upper bounds for CO<sub>2</sub>/CH<sub>4</sub> and CO<sub>2</sub>/N<sub>2</sub> separations using a series of ultrapermeable benzotriptycene-based polymers of intrinsic microporosity. *Energy Environ. Sci.* **2019**, *12*, 2733–2740. [[CrossRef](#)]
51. Friess, K.; Jansen, J.C.; Bazzarelli, F.; Izák, P.; Jarmarová, V.; Kačírková, M.; Schauer, J.; Clarizia, G.; Bernardo, P. High ionic liquid content polymeric gel membranes: Correlation of membrane structure with gas and vapour transport properties. *J. Membr. Sci.* **2012**, *415–416*, 801–809. [[CrossRef](#)]
52. Mousa, M.; Dong, Y. The role of nanoparticle shapes and structures in material characterization of polyvinyl alcohol (PVA) bionanocomposite films. *Polymers* **2020**, *12*, 264. [[CrossRef](#)]